



HAL
open science

A fibrous cellulose paste formulation to manufacture structural parts using 3D printing by extrusion

C. Thibaut, A. Denneulin, S. Rolland Du Roscoat, D. Beneventi, L. Orgeas,
D. Chaussy

► To cite this version:

C. Thibaut, A. Denneulin, S. Rolland Du Roscoat, D. Beneventi, L. Orgeas, et al.. A fibrous cellulose paste formulation to manufacture structural parts using 3D printing by extrusion. Carbohydrate Polymers, 2019, 212, pp.119-128. 10.1016/j.carbpol.2019.01.076 . hal-02021646

HAL Id: hal-02021646

<https://hal.univ-grenoble-alpes.fr/hal-02021646>

Submitted on 22 Oct 2021

HAL is a multi-disciplinary open access archive for the deposit and dissemination of scientific research documents, whether they are published or not. The documents may come from teaching and research institutions in France or abroad, or from public or private research centers.

L'archive ouverte pluridisciplinaire **HAL**, est destinée au dépôt et à la diffusion de documents scientifiques de niveau recherche, publiés ou non, émanant des établissements d'enseignement et de recherche français ou étrangers, des laboratoires publics ou privés.



Distributed under a Creative Commons Attribution - NonCommercial 4.0 International License

1 A fibrous cellulose paste formulation to
2 manufacture structural parts using 3D printing by
3 extrusion

4 *C. Thibaut^{‡‡}, A. Denneulin[‡], S. Rolland du Roscoat[†], D. Beneventi[‡], L. Orgéas[†] and, D. Chaussy^{‡*}*

5 [‡]Univ. Grenoble Alpes, CNRS, Grenoble INP^a, LGP2, F-38000 Grenoble, France

6 [†]Univ. Grenoble Alpes, CNRS, Grenoble INP^a, 3SR, F-38000 Grenoble, France

7 *corresponding author:

8 mail: didier.chaussy@grenoble-inp.fr

9 tel: +33 (0)4 76 82 69 08

10 address: 461, rue de la Papeterie, CS 10065, 38402 Saint-Martin-d'Hères Cedex - France

11 Abstract

12 An optimized paste based on short natural cellulose fibers combined with carboxymethyl cellulose at a
13 high dry content (42 wt.%) was implemented as a bio-based material for 3D printing by extrusion. The
14 homogeneous paste exhibited a pronounced thinning behavior and yield stress; it was extruded using a
15 screw extrusion-based direct ink writing system and could easily flow through a small nozzle. The

^a Institute of Engineering Univ. Grenoble Alpes

16 optimized formulation enabled accurate additive manufacturing of parts using a natural air-drying
17 process with or without an ethanol bath. We characterized the anisotropic shrinkage that occurred
18 during the drying of 3D printed parts and proposed a compensation method to account for it. The
19 obtained results emphasized that cellulose had a strong potential to be used as a raw material for 3D
20 printing of cheap, lightweight, robust, and recyclable parts.

21 **Keywords:** 3D printing; cellulose; extrusion; bio-based material

22 **1. Introduction**

23 Additive manufacturing, often referred as 3D printing, is regarded as a disruptive technology with
24 many application fields, including the automotive industry, medical field, and leisure sector. This process
25 of joining materials is used to fabricate objects from 3D model data, usually layer upon layer, as opposed
26 to subtractive manufacturing methodologies. Additive manufacturing comprises a wide range of
27 different technologies, as described by ASTM International (2012), each with their own advantages and
28 drawbacks. In general, the additive manufacturing process offers new design opportunities for complex
29 and lightweight designs, short manufacturing lead times, and simple design modifications (Huang, Liu,
30 Mokasdar, & Hou, 2013). This technology is compatible with a broad range of materials, such as metals,
31 polymers, ceramics, gels, food, and bio-based materials (Wohlers, Caffrey, & Campbell., 2016).

32 Cellulose in the form of fibers, which is the most abundant bio-based polymer on earth with excellent
33 mechanical properties (Dufresne, 2013), may be a very promising candidate for producing cheap,
34 lightweight, robust, and recyclable 3D structures by 3D printing: It may be used not just as an additive
35 for mechanical reinforcement **or as** a rheological modifier, **but also** for **many** other applications, as
36 discussed in a recent review on 3D printing cellulose and its derivatives (Dai et al., 2019). Indeed, up to
37 now, the potential uses of cellulose as a bulk material for 3D printing have not been fully explored
38 (Wang et al., 2018). Additive manufacturing with cellulose as the main building block has been reported

39 for three categories of additive manufacturing processes of the seven defined by ASTM International
40 (2012): Binder jetting (Sachs, Cima, Williams, Brancazio, & Cornie, 1992), sheet lamination (Feygin &
41 Hsieh, 1991) and, material extrusion (US5121329A, 1992). This last process is promising because it
42 allows the manufacture of complex and light parts with more than one material, unlike the binder
43 jetting and sheet lamination processes. Thermoplastic polylactic acid (PLA), which is derived from starch,
44 has been considered as a material reference for this study regarding the 3D printing material extrusion
45 process due to its easy processing and extensive use (Steinle, 2016; Wittbrodt & Pearce, 2015).

46 It was only twenty years after the development of this 3D printing extrusion process, that cellulose
47 was used for the first time to 3D print part by this process (based on our knowledge, Markstedt,
48 Sundberg, & Gatenholm, 2014). It comes from the various challenges raised by the properties of
49 cellulose and of this process. Unlike thermoplastic materials, which are compatible with 3D printing by
50 melt extrusion, cellulose cannot be melted to be processed and so recover its stiffness when cool down.
51 Thus, a solvent must be added to precisely control the filament extrusion during the forming step and to
52 achieve higher accuracy of the 3D printed parts. The successful extrusion of a filament has three
53 requirements: (i) a constant extrusion flow must be set which does not cause nozzle clogging or filament
54 breaking under a constant pressure, (ii) the filament produced must have a homogeneous composition
55 with a constant diameter, and (iii) the pressure required to force the material through the nozzle must
56 be within the capabilities of the equipment used. After printing, the part must stand upright. Thus, the
57 viscosity of the material should be sufficiently high. Finally, the part generally needs to be dried
58 depending on the intended use and final properties. Quantitative indicators to assess the printability
59 and shape fidelity of 3D printed part with a new developed formulation area current area of study
60 (Wang et al., 2018).

61 Recently, several articles have been published on formulations compatible with 3D printing by
62 extrusion with cellulose as the main building block. Herein, we are interested in formulations that can

63 achieve high-definition printing with nozzle diameters around 500 μm , and thus, formulations that
64 require large nozzles are not presented (Sanandiya, Vijay, Dimopoulou, Dritsas, & Fernandez, 2018).
65 These formulations can be divided into two groups: dissolved cellulose and cellulose suspensions.
66 *Dissolved cellulose:* Markstedt, Sundberg, & Gatenholm, 2014 used cellulose fibers dissolved in an
67 ionic liquid (EmimAc (1-ethyl-3-methylimidazolium acetate)). One limitation was the solid content of
68 their solutions (4 wt.%), which limited the pressure for the extrusion to 6 bars for their operating
69 parameters (12.7 mm long needle with an inner diameter of 0.41 mm at a flow rate of 10 $\mu\text{L}/\text{min}$).
70 Subsequently, they had to balance the rate of coagulation. If the coagulation occurred too quickly, there
71 was poor adhesion between printed layers. However, if the coagulation occurred too slowly, there was a
72 height limitation of the printed part to avoid its collapse L. Li, Zhu, & Yang, (2018) dissolved cellulose
73 fibers in N-nethylmorpholine N-oxide (NMMO) at less than 10 wt.%. Their **solution** was printed at 70 $^{\circ}\text{C}$
74 and solidified after the extrusion, similar to the fused filament fabrication (FFF) method. Parts were
75 successfully printed with heights around 1 cm. The printed part was freeze-dried to maintain the
76 interconnected porous structures in the final product. Pattinson & Hart, 2017 used cellulose acetate at
77 25-30 wt.% in acetone. The quasi-immediate evaporation of the acetone (~ 1 min) during the printing
78 allowed **(i)** the hardening of the part as it was printed **and**, **(ii)** the shrinkage compensation of every
79 printed layer to maintain dimensional stability of the part. The main drawback of this approach was the
80 speed limitation due to the acetone evaporation process.

81 *Suspension of cellulose:* Cellulose in its nanostructured form was dispersed in water with or without
82 chemical modifications and, in some cases, with the addition of alginate at a very low concentration (<5
83 wt.%) (Chinga-Carrasco et al., 2018; Håkansson et al., 2016; V. C. F. Li, Mulyadi, Dunn, Deng, & Qi, 2018;
84 Markstedt et al., 2015; Rees et al., 2015; Sultan & Mathew, 2018) and at larger concentration (around
85 20 wt.%) (Jia et al., 2017; Klar, Kärki, Orelma, & Kuosmanen, 2017; V. C.-F. Li, Dunn, Zhang, Deng, & Qi,
86 2017; Siqueira et al., 2017). The suspensions were successfully extruded through small nozzles and

87 deposited on a substrate to form parts of about 1 cm³ with height from 0.2mm up to 30 mm to
88 demonstrate the printability of the suspensions. Due the small sizes of the printed parts in most studies,
89 these previous reports cannot assess (i) the absence of clogging issues due to nanocellulose aggregation
90 in the nozzle nor (ii) the height limitations due to viscosities that are too small to resist the weight of the
91 parts. Compared to acetone, the water evaporation rate at ambient conditions is low. Yet, the hardening
92 and main deformation begins after completion of the 3D printed part. In general, these printed parts
93 were used either in their wet states after cross-linking with solutions, such as CaCl₂ solutions, or were
94 freeze-dried to produce porous media and preserve the 3D structure of the printed part. Håkansson et
95 al., 2016 evaluated three other drying techniques less expensive than freeze drying for preserving the
96 3D structure and dimensions of printed parts with 2 wt.% nanocellulose suspensions in water: solvent
97 exchange, addition of surfactant and air drying. Solvent exchange or addition of surfactant, which added
98 a post-treatment step, only preserved the 3D structures of the parts whereas the air-drying technique
99 did not preserve the 3D structure and dimensions. However, with a high-concentration nanocellulose
100 suspension (22 wt.%), Klar, Kärki, Orelma, & Kuosmanen, 2017 successfully preserved the 3D structures
101 and obtained an 80% volume shrinkage (i.e. around 5% porosity) after natural air drying. This large
102 amount of shrinkage prevented compensation methods from being used. To compensate for the
103 shrinkage, the volume of the 3D model part should be multiplied by five, which strongly impacts the
104 printing time. Moreover, this printing time might be larger than the drying time of the first layers for
105 large parts, causing shrinkage to begin before printing is complete, which can lead to printing failure.

106 These developed formulations with cellulose as the main component raised several questions: Can
107 cellulose be a new, cheap, lightweight, robust, renewable, and biodegradable material compatible for
108 3D printing by extrusion similar to PLA? What form of cellulose (natural cellulose fiber, nanocellulose,
109 cellulose derivative) should be used and with which solvent? What proportion of cellulose fibers is
110 required to limit deformation after drying and the cost of the drying process while being an extrudable

111 material? Are there any design restrictions or new design opportunities compared to fused filament
112 fabrication processes with thermoplastic materials, such as the bio-based PLA?

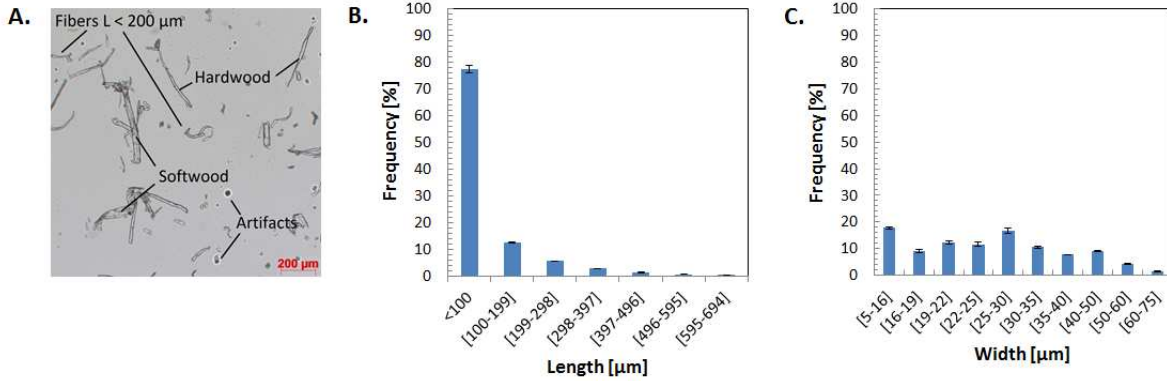
113 Herein, we report a new formulation based on natural cellulose fibers and a cellulose derivative that is
114 compatible with extrusion-based 3D printing and a natural air-drying process with or without a solvent
115 exchange step with ethanol. This formulation and process resulted in limited and anisotropic
116 deformation that allowed the use of a compensation strategy. This new formulation easily flowed
117 through the small nozzle and exhibited suitable specific mechanical properties after drying. We
118 successfully printed complex parts and compensated for height deformation due to drying to maintain
119 fidelity with the initial 3D digital model. The obtained printed parts were compared to parts obtained
120 with PLA, the benchmark for 3D printing by extrusion of bio-based materials.

121 **2. Experimental procedure**

122 **2.1 Material and paste preparation**

123 A cellulose-based paste was prepared by dry mixing natural cellulose fibers and carboxymethyl
124 cellulose (CMC) and adding distilled water.

125 - The cellulose fibers (Carl Roth) consisted of a mix of milled hardwood and softwood natural fibers,
126 as illustrated in Figure 1A. The fiber length and width distributions were measured using the
127 Morfi[®] approach (Techpap[®], Grenoble, France) (Passas, R., Voillot, C., Tarrajat, G., Khélifi, B., &
128 Tourtollet, G., 2001). Figure 1B and C show that (i) 90% of the fibers were shorter than 200 μm
129 and (ii) fibers longer than 100 μm had a mean fiber width of 27 μm , respectively.



130

131 Figure 1. Optical characterization of cellulose fibers. (A) Image of natural cellulose fibers in
 132 suspension. (B) Length distribution of cellulose fibers. (C) Width distribution of cellulose fibers with
 133 lengths greater than 100 μm .

134

135 - Sodium CMC with an average molecular weight of 90,000 and 0.7 carboxymethyl groups per
 136 anhydroglucose unit was purchased from Sigma Aldrich.

137 Batches of 100 g of the cellulosic paste were prepared with a CMC/fiber mass ratio ranging from 0.13
 138 to 1.33, after which distilled water was added to adjust the dry solid contents. The paste was
 139 homogenized for 5 min at 120 rpm using a planetary mixer (Proline RP10). The paste was stored for 24 h
 140 in a refrigerator at 4–5 $^{\circ}\text{C}$ before printing.

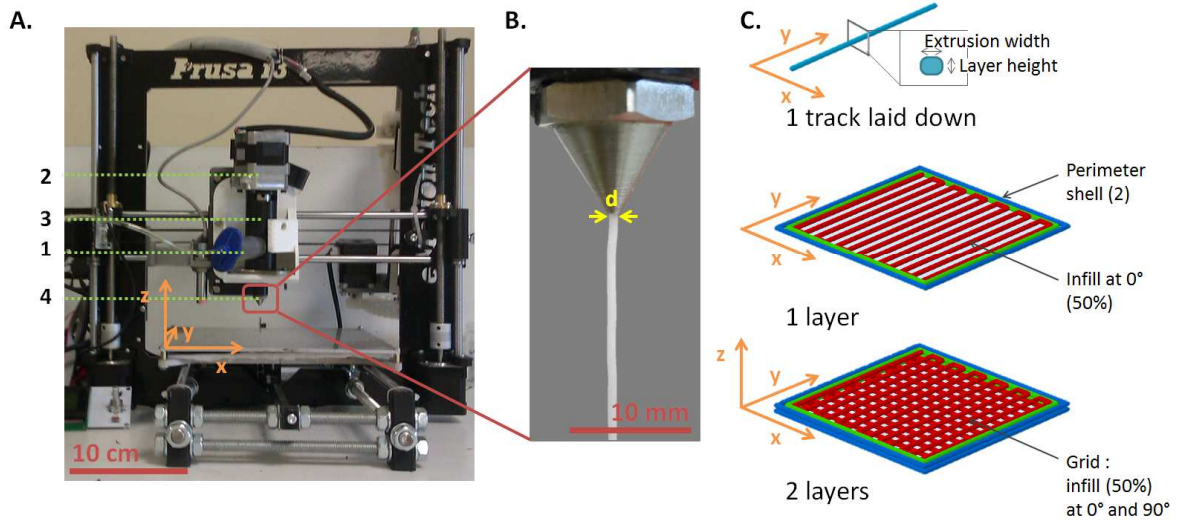
141 The formulations had overall dry contents varying from 35 to 50 wt.%, cellulose fiber contents varying
 142 from 15 to 45 wt.%, and CMC contents varying from 5 to 20 wt.%. These ratios were chosen after
 143 preliminary testing to achieve a balance between the extrusion processes of the paste, increase the solid
 144 content in the cellulose fibers to limit the shrinkage upon drying, and increase the CMC content to
 145 promote fiber dispersion by increasing the viscosity of the distilled water.

146

147 **2.2 3D printing by extrusion**

148 *Printer:* A commercial 3D printer Prusa i3 was upgraded with a liquid deposit modeling (LDM) WASP
149 extruder (Figure 2.A). An air pressure syringe (caption 1 of Figure 2A) was used to feed the cavity of the
150 LDM extruder with the paste described in Section 2.1. This cavity was placed in the device just before
151 the paste entered the LDM extruder. The extruder consisted of a screw-driven device (2) in a barrel (3)
152 and a steel nozzle (4) with an outlet diameter d varying from 0.5 to 0.9 mm. The inner shapes of the
153 nozzles were designed with two successive constrictions from a diameter of approximately 5 mm to the
154 final outlet diameter d . This device could apply up to 40 bar of pressure to the paste, a significantly
155 higher pressure than the typical 7 bar pressures achieved by pneumatic extruders. This LDM extruder
156 allowed the use of highly viscous pastes at printing speeds of the same order of magnitude as those of
157 the FFF process, ranging from 10 to 50 mm s⁻¹. It was possible to quickly interrupt the flow by changing
158 the direction of the screw rotation to release the pressure applied to the paste. To compensate for the
159 pressure loss due to the nozzle, the rotational velocity of the screw was set 2 to 3 times larger than the
160 pressure used when the nozzle was absent to achieve the flow required for accurate 3D printing. The
161 rotation velocity of the screw was approximately 10 rpm during printing.

162



163

164 Figure 2. (A) 3D printer Prusa i3 upgraded with a Liquid Deposit Modeling WASP Extruder. (1) Air
 165 pressure syringe, (2) screw-driven device, (3) barrel, and (4) steel nozzle. (B) Close-up of nozzle with an
 166 inner diameter of 0.7 mm. Smooth filaments could be extruded without apparent swelling. (C)

167 Visualization obtained using Simplify 3D of one track, one layer, and two layers of a cube

168

169 *Printed parts:* In general, to 3D print a part, a CAD model is first sliced orthogonally in the z direction
 170 in thin layers, which are then divided into tracks by a slicing software (Simplify 3D in this study) using
 171 several key parameters: (i) the extrusion width (thickness of the track laid down), (ii) the layer height
 172 (thickness of each layer), (iii) the infill (density of rectilinear pattern in one layer), and (iv) the perimeter
 173 shell (solid wall of the model). These parameters are illustrated in Figure 2C. This dataset and the
 174 printing speed are converted to a programming language compatible with the printer. One layer at a
 175 time, the extruder head (and/or the build platform on which the part is manufactured) moves in the
 176 (x,y) plane and extrudes material shaped as a flatten filament in order to create one cross-section of the
 177 part. After completing the layer, the extruder head lifts (or the building plate lowers) to the height of a
 178 layer thickness to build the next layer of the part on top of the previous layer, and this process continues
 179 until the part is completed. Various geometrical parts (2D and 3D) were printed using the upgraded

180 printer and pastes described in Section 2.1. First, single filaments of 100 and 200 mm were extruded
 181 using a 0.7 mm diameter nozzle at a linear flow ranging from 3 to 5 mm s⁻¹ at approximately 20 cm
 182 above the printing surface. Figure 2B shows the typical filaments obtained. Five different geometric
 183 models with increasing complexity were tested: (i) a 6 cm³ cube; (ii) a 4.0 cm high monofilament
 184 rectangular cuboid with a 4.00 cm² square cross-section; (iii) a 1.5 cm long bridge with a 1 cm high pillar
 185 and rectangular cross-section of 0.5 × 1.0 cm²; (iv) a 3DBenchy model composed of complex 3D printing
 186 shapes, including a 40° overhang, 1.0–2.0 cm bridge, and 1 cm high narrow pillar with a 0.15 cm² cross-
 187 section; and (v) a 5.0 cm high double spiral vase with an opening diameter of 1.6 cm. Models (iv) and (v)
 188 were downloaded from the Thingiverse database (Thingiverse.com, March 2018). The printing
 189 parameters are given in Table 1.

3D model name	Cube	Monofilament rectangular cuboid		Bridge	3DBenchy	Double spiral vase
Nozzle diameter [mm]	0.7	0.7	0.9	0.5	0.5	0.5
Extrusion width [mm]	0.7	0.7	0.9	0.5	0.5	0.5
Layer height [mm]	0.56	0.56	0.70	0.40	0.30	0.30
Printing speed [mm s ⁻¹]	10		10	10	20	15
Infill [%]	50		0	100	50	100
Perimeter shell	2		1	2	2	2

190

191 **Table 1.** 3D printing parameters

192 *Drying:* Once printed, the samples (filament and 3D parts) were dried using two different methods.
 193 They were either (i) conditioned at 23 °C and 50% relative humidity for 48 h or (ii) immersed in an
 194 ethanol (95%) bath for 2 h (30 min for extruded filament) to exchange the solvent with a lower surface
 195 tension solvent, as reported by Håkansson et al., 2016, followed by conditioning (as described in (i)).

196 During the drying process, the filament was suspended from the support for at least 30 min to avoid
197 friction. The length of this filament was short enough to prevent it from stretching under its own weight.

198 *Dimension measurements:* After drying, the dimensions of the printed filaments and 3D parts were
199 measured. To measure the filament diameters, three images per filament were taken with a binocular
200 magnifier at $\times 100$ (ZEISS SteREO Discovery V20 with an AxioCam ICc 5) with a pixel size of $0.54\ \mu\text{m}$, two
201 centimeters apart all along the filament length. The obtained pictures were analyzed using the imageJ
202 “Analyze stripes v2.4.5.b” plugin (Copyright 2013 Justin R. Bickford) to measure the distance between
203 the edges of the filament, which was considered to be the filament diameter. The filament length was
204 measured with a graduated ruler ($\pm 0.05\ \text{cm}$). The height of the monofilament cuboid was measured
205 with a digital caliper ($\pm 0.01\ \text{mm}$) at the four edges of the cuboid and at four central points between two
206 consecutive edges to obtain the mean value and standard deviation. The height and outlet diameter of
207 the dried double spiral vase were measured with the same digital caliper. The areas of the holes of the
208 50% infilled $6\ \text{cm}^3$ cube were measured on the undried region: (i) an image of the $6\ \text{cm}^3$ cube just after
209 completion of the printing ($< 5\ \text{min}$) was taken with the binocular magnifier at $\times 7.5$ with a pixel size of 7
210 μm and (ii) the dark holes of the grid were counted and their area measured using imageJ.
211 Measurements were performed on 56 holes.

212 *Weight measurement:* After the filaments were dried and their dimensions were measured, three
213 filaments were stored for 48 h in a conditioned room at $23\ ^\circ\text{C}$ and 50% RH, after which they were
214 weighed to within $\pm 0.0001\ \text{g}$.

215 **2.3 Characterization**

216 **2.3.1 Rheology of the pastes**

217 To characterize the rheology of the cellulosic pastes in the “fresh” state, *i.e.*, at the nozzle exit, we
218 performed lubricated squeeze flow tests using a universal tension-compression testing machine
219 equipped with a 2 kN load cell (Instron 5944). These tests are well-suited to study the rheology of highly
220 viscous pastes reinforced with fibers of finite lengths. Indeed, characterizing the rheology of such (fiber-
221 reinforced) pastes using standard shear or high pressure capillarity rheometers may be difficult due to (i)
222 the size of fibers (Chalencon et al., 2010; Orgéas, Dumont, Le, & Favier, 2008) and (ii) their marked shear
223 thinning, which often causes to undesirable wall slippage and shear banding (Martoïa et al., 2015)
224 (Orgéas, Gabathuler, Imwinkelried, Paradies, & Rappaz, 2003). We prepared cylindrical samples from
225 the pastes with initial heights $h_0 = 7$ mm and diameters $d_0 = 10$ mm. Each sample was placed between
226 two parallel compression plates that were lubricated with thin layers of a mixture of silicon oil and
227 grease to ensure a homogeneous compression flow of the sample. The samples were monitored with a
228 video camera. The recorded videos showed that samples flowed at nearly constant volume (less than 2%
229 of volume variation of the cylinder at the end of the tests). Using the compression force F
230 measurements and the actual sample height h , we plotted the evolution of the compression Cauchy
231 stress, $|\sigma| = 4|F|/h/\pi h_0 d_0^2$, with time t and with the compression Hencky strain, $|\varepsilon| = |\ln h/h_0|$. The
232 tests were first carried out at constant compression velocity \dot{h} and with initial compression strain rates
233 $|\dot{\varepsilon}_0|$ ranging from 0.01 to 1 s^{-1} , up to a compression strain $|\varepsilon| = 0.8$. Subsequently, the compression
234 ended and the stress relaxation was recorded for 2 mins, *i.e.*, up to steady-state regimes with
235 approximately constant stresses. Three samples were used for each testing condition, and the error bars
236 given in the following graphs correspond to the min and max values recorded during these tests.

237 **2.3.2 Deformation after drying**

238 The deformation was calculated as the absolute value of the engineering strain $|e| = |X_{\text{dried}}/X_{\text{fresh}} - 1|$,
239 where X_{dried} corresponds to the measurements obtained using the methods described in the *Dimension*

240 *measurements* section in Section 2.2 and X_{fresh} corresponds to (i) the dimensions given in the *Printed*
241 *part* section in Section 2.2 or (ii) the nozzle diameter for transversal strain of the filament, as no
242 apparent swelling was observed. The longitudinal and transversal strains of the filament diameter were
243 calculated for each formulation on three air dried 10.0 ± 0.2 cm long filaments extruded through the 0.7
244 mm diameter nozzle at an output flow of 3 mm s^{-1} . The strain of the 4 cm high monofilament cuboid was
245 calculated for each formulation with two air dried samples. The strain of the vase was calculated on a
246 single sample.

247 **2.3.3 SEM observations**

248 To characterize the microstructures of the extruded filaments, two types of samples were recorded:
249 (i) filaments dried with or without an ethanol bath with cross-sections cut using a razor blade with an
250 angle of approximately 45° and (ii) air dried filaments after the tensile tests. Samples cut with the razor
251 blade were metalized with a thin layer of gold and palladium (around 1 nm) and the tensile tested
252 sample was metalized with carbon. Then, SEM images of the surface and cross-section of the filament
253 were recorded on a FEI Quanta 200.

254

255 **2.3.4 Tensile test**

256 To characterize the mechanical properties of the paste after drying, we performed tensile tests with a
257 universal tension-compression testing machine (Instron 5965) equipped with a 5 kN load cell in a
258 conditioned room (23°C , 50% RH). We prepared filament samples that were extruded through a 0.7
259 mm diameter nozzle at an output flow of 4.5 mm s^{-1} and dried with or without solvent exchange in
260 ethanol. The initial diameters of the dried samples were measured by an image analysis (Section 2.2
261 *Dimension measurements*, measurement of filament diameter) with a 10 cm gage length. As discussed in
262 Section 2.3.1, we plotted the Cauchy stress as a function of the Hencky strain, which can be
263 approximated from the engineering strain for small deformations. The tests were carried out at a

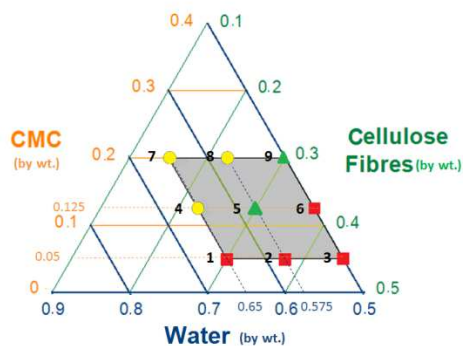
264 constant stretch velocity of 10 mm min^{-1} until filament breakage. Five samples were measured for each
 265 drying condition.

266 3. Results and discussion

267 3.1 Optimization of the formulation of the cellulose-based paste for 3D printing by 268 extrusion

269 To identify an optimized cellulose-based paste formulation compatible with 3D printing by extrusion,
 270 several pastes with varying solid contents and proportions of compounds were evaluated.

A.



B.

Caption	Monofilament cuboid (20*20*40 mm ³)	N° Formulation	Cuboid height → deformation	Diameter of filament → deformation	Length of filament → deformation
Not compatible with 3D printing by extrusion		1	-	-	-
		2	-	-	-
		3	-	-	-
		6	-	-	-
Partially compatible with 3D printing by extrusion		4	24±1 mm → 41±2%	0.48±0.04 mm → 34±5%	91±1 mm → 9±2%
		7	23±1 mm → 43±3%	0.44±0.02 mm → 38±3%	95±1 mm → 5±2%
		8	25±1 mm → 39±3%	0.48±0.02 mm → 33±3%	95±1 mm → 5±2%
Compatible with 3D printing by extrusion		5	26±1 mm → 34±3%	0.51±0.01 mm → 30±1%	97±1 mm → 3±2%
		9	27±1 mm → 32±4%	0.53±0.01 mm → 27±2%	97±1 mm → 3±2%

271

272 Figure 3. (A) Ternary diagram indicating the weight fractions of CMC, cellulose fibers, and water for the
 273 tested formulations. (B) Qualitative and quantitative characterization of the nine different tested
 274 formulations for compatibility with 3D printing by extrusion.

275 Figure 3A shows the compositions of the nine tested formulations. These formulations were assessed
 276 according three main criteria, which ensured the accuracy of the printed part relative to the 3D model:
 277 (i) extrusion of an adequate filament, as defined in the Introduction; (ii) production of undried and
 278 accurate 3D printing parts that do not collapse; and (iii) limiting and forecasting the deformation after
 279 drying. These criteria were applied to a 10 cm long filament and the monofilament cuboid part that was
 280 extruded, printed, and air dried using the parameters specified in Section 2.2 and in Table 1.

281 Figure 3B shows the typical results obtained with the nine tested formulation, which were as follows:

- 282 - The tested formulations with cellulose fiber contents of 37.5 wt.% or with a CMC content at 5
283 wt.% did not allow the extrusion of smooth and regular filaments with a nozzle diameter of 0.7
284 mm, as the extruded filaments were friable and irregular, which led to filament breakage.
285 Furthermore, these characteristics did not allow the complete printing of a regular monofilament
286 wall cuboid, as can be seen in Figure 3B. These formulations were found to be incompatible with
287 3D printing by extrusion, as they did not meet criteria (i) based on filament extrusion, and (ii)
288 based on the accuracy of the undried 3D printed part.
- 289 - The five remaining tested formulations with cellulose fiber contents of 30 wt.% or less and a CMC
290 content of 12.5 wt.% or more yielded smooth and regular filaments extruded through a 0.7 mm
291 diameter nozzle, allowing the manufacture of a monofilament cuboid as high as 4 cm with a wall
292 thickness of the size of the nozzle outlet, as no die swelling was observed. These parts did not
293 collapse under their own weights, as can be seen in Figure 3B. Indeed, the lower region of the 3D
294 part did not widen. However, the stacked extruded filaments were not perfectly aligned. This
295 misalignment might be due to a small amount of over-extrusion or a small displacement of the
296 corner caused by the motion of the nozzle and the extruded paste that generates imperfections or
297 the buckling of the thin walls under the pressure caused by the extruded paste (Buswell, Leal de
298 Silva, Jones, & Dirrenberger, 2018; Suiker, 2018). These five formulations were found to be
299 compatible with 3D printing by extrusion to manufacture wet parts, as they met criteria (i) based
300 on adequate filament extrusion, and (ii) based on the accuracy of the undried 3D printed part.
- 301 - Figure 3B also summarizes the strain of the extruded filament and the height of the cuboid after
302 drying. For formulations with a cellulose fiber content lower than 30 wt.%, the strains of the
303 filaments were larger than 30% and 5% for the diameters and lengths, respectively, and the height
304 strain of the cuboid was larger than 35%. Therefore, these formulations with cellulose fiber

305 contents lower than 30 wt.% were found to be partially compatible with 3D printing by extrusion
306 because of the high strain observed after drying (criteria (iii)). By comparison, the formulations
307 containing 30 wt.% of cellulose fibers and CMC contents of 12.5% or 20 wt.% exhibited better
308 strain behaviors during the drying phase. These two last formulations were found to be
309 compatible with 3D printing by extrusion, as they fulfilled criteria (i) based on adequate filament
310 extrusion, (ii) based on the accuracy of the undried 3D printed part and, and (iii) based on
311 limitation of the deformation after drying.

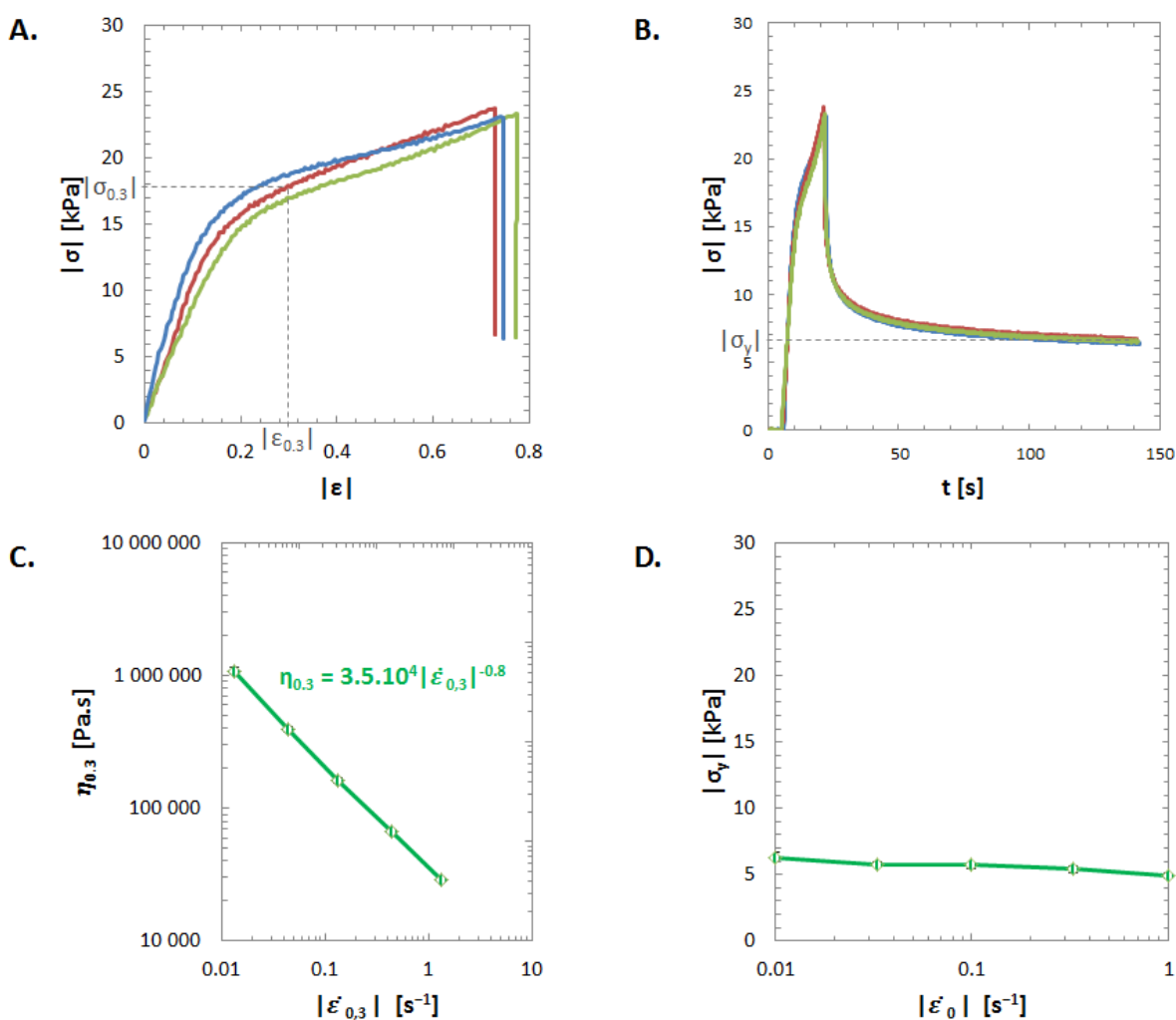
312 To conclude, the formulation with a dry content of 42.5 wt.%, a cellulose fiber content of 30 wt.%, and
313 a CMC content of 12.5 wt.% was selected as the optimized formulation, because its cost was lower than
314 a similar formulation in which 7.5 wt.% of distilled water was replaced by CMC, and because the paste
315 that was formed was easily processed, facilitating simple filling of the syringe (Appendix 1). This
316 optimized formulation was equivalent to a solid content of 23.3 vol.% based on the cellulose fiber
317 density of 1.5 g cm^{-3} in a CMC gel at 0.22 g mL^{-1} . This cellulose fiber solid content was two times lower
318 than the solid content used in the other two pastes successfully formulated for 3D printing by extrusion
319 at ambient temperature with a nozzle diameter smaller than $500 \mu\text{m}$: (i) 45 vol.% of glass powder with
320 up to 2 wt.% of CMC (Eqtesadi et al., 2013) and (ii) 47 vol.% of lead zirconate titanate and a cellulose
321 concentration of 5 mg mL^{-1} (Smay, Cesarano, & Lewis, 2002). This difference in solid content might arise
322 from the components used. The glass powder and lead zirconate titanate were unlike cellulose fibers, as
323 they had smaller dimensions ($< 10 \mu\text{m}$), round geometries, and low interactions with water (e.g.
324 hydrogen bonding or hygroexpansion). Using an elongated cellulose mat, V. C. F. Li et al., 2018 and
325 Siqueira et al., 2017 also successfully formulated a paste at high solid content with 20 wt.% of freeze-
326 dried cellulose nanocrystals (CNCs) as received or modified CNC in suspension. They limited their solid
327 content to 20 wt.% owing to limitations of the devices used for mixing and/or printing, which did not
328 allow proper homogenization of the paste or sufficient extrusion flow or alignment of the CNCs. These

329 solid contents were lower than the optimized formulation (30 wt.% of cellulose fibers) proposed herein.
 330 These differences were due to the use of a screw-driven device instead of a pneumatic device and the
 331 addition of CMC, which reduced the friction between fibers.

332 3.2 Characterization of the optimized formulation

333 In the following section, we discuss the properties of the optimized paste.

334 3.2.1 Rheological behavior of the fresh paste



335
 336 Figure 4. Rheological properties of the optimized formulation (30 wt.% cellulose fiber, 12.5 wt.%
 337 carboxymethyl cellulose, 57.5 wt.% distilled water). Three lubricated squeeze flow tests (compression at

338 constant speed followed by 2 min of relaxation) were performed at an initial compression strain rate of
339 0.033 s^{-1} . (A) Stress-strain curves. (B) Stress during the lubricated squeeze flow test. During the
340 relaxation time, the stress reached a plateau, which corresponds to the yield stress $|\sigma_y|$. (C) Viscosity
341 curve fit with a power law, $\eta_{0.3} = k|\dot{\epsilon}_0|^{n-1}$. (D) Yield stress $|\sigma_y| = 6 \text{ kPa}$ as a function of the initial strain
342 rate.

343 Figure 4A and B show typical stress-strain and stress-time curves recorded with the optimized
344 formulation during three compression tests, which were obtained at a first compression flow of $3.33 \cdot 10^2$
345 s^{-1} . Similar curves were obtained for the formulation listed as compatible in Figure 3B. High
346 reproducibility of the stresses was observed, with deviations of less than $\pm 10\%$. After a quasi-linear and
347 sharp increase of the stresses, the samples flowed more easily, exhibiting stress hardening behaviors
348 that are typical of fiber-reinforced paste materials (Chalencon et al., 2010; Orgéas et al., 2008).

349 We arbitrarily characterized the transition between these two regimes using the compression stress
350 $|\sigma_{0.3}|$ recorded at a compression strain $|\epsilon| = 0.3$. As shown in Figure 4C, the compression viscosity $\eta_{0.3} =$
351 $\sigma_{0.3}/\dot{\epsilon}_{0.3}$ decreased with the strain rate $|\dot{\epsilon}_{0.3}|$ and followed a power-law function, *i.e.*, $\eta_{0.3} = k|\dot{\epsilon}_{0.3}|^{n-1}$. The
352 value obtained for the power-law exponent, $n = 0.2$, indicates the optimized pastes exhibited a
353 pronounced thinning behavior, which is similar to those obtained for similar fiber-reinforced paste
354 materials. The stress levels recorded here one order of magnitude higher than those reported under
355 shear for other 3D printing formulations (Compton & Lewis, 2014; Lewis, 2006; Siqueira et al., 2017;
356 Smay et al., 2002).

357 When the compression flow stopped, the compression stress rapidly decreased to reach a steady and
358 constant stress (Figure 4B), which corresponds to the yield stress $|\sigma_y|$ after the paste flow. Figure 4D
359 shows that $|\sigma_y|$ achieved finite values that were independent of the initial strain rate $|\dot{\epsilon}_0|$ (Figure 4D).
360 The yield stress $|\sigma_y|$, which was measured for the “fresh” state, is one of the most critical parameters
361 for 3D printing from a mechanical standpoint (as the paste liquid phase evaporates, the yield stress is

362 expected to increase). If the stress state in a “fresh” printed filament remains below the yield stress, the
363 filament should behave as an elastic solid and maintain its printed shape. Above this value of yield
364 strength, the dimensional stability may be lost, as the paste can flow.

365 **3.2.2 Shrinkage during drying**

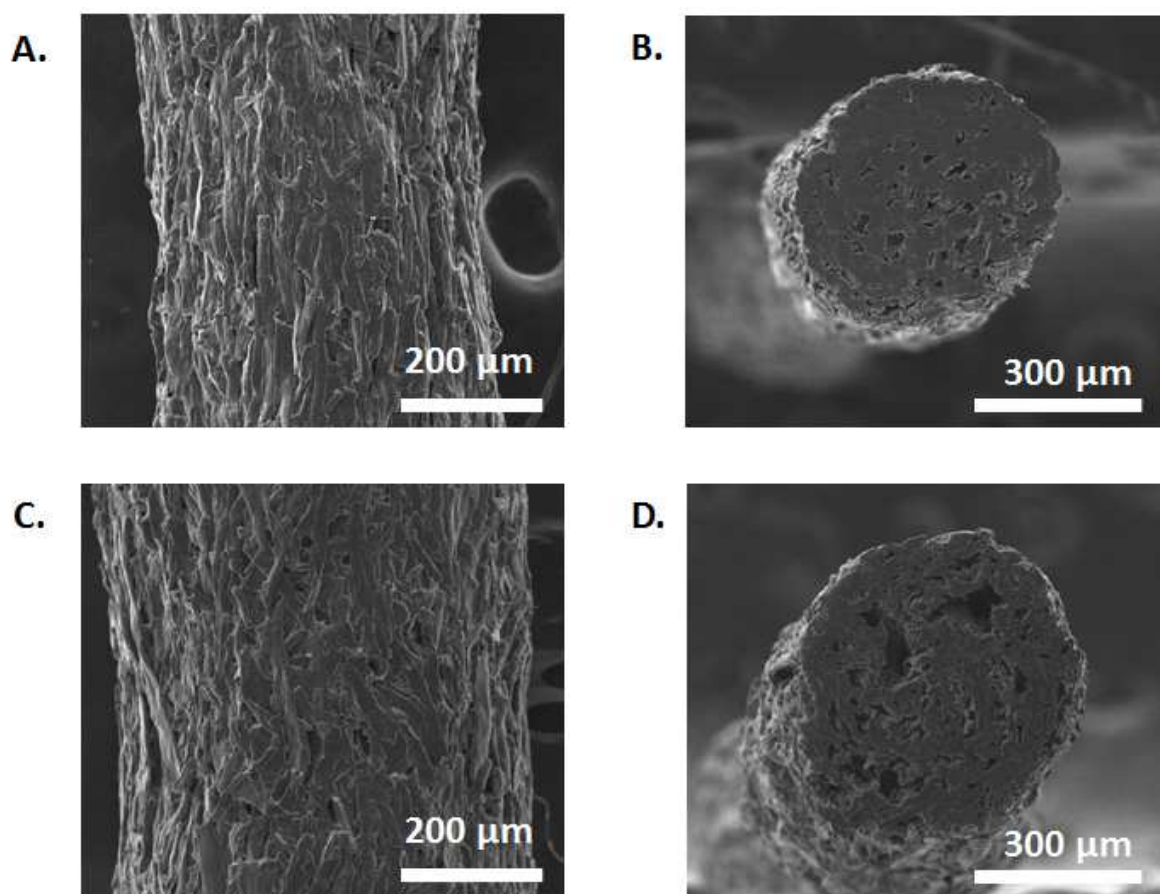
366 As illustrated in Figure 3B, after drying, the filament diameter and length decreased. The filament
367 diameter decreased from 0.72 to 0.49 ± 0.1 mm, and its length decreased from 200 to 193 mm. The
368 strain was primarily radial. These dimensional changes were due to the 57.5 wt.% of distilled water in
369 the optimized paste. During the drying phase, the water must evaporate. During this process, water is
370 transported from the inside to the outside of the printed part, leading to high drying stresses, such as
371 the capillarity pressure (Scherer, 1990). The capillary forces tend to bring the cellulose fibers embedded
372 in dissolved CMC closer together (i.e. mainly in their longitudinal direction), resulting in strain.
373 Moreover, the hygroexpansion of a cellulose fiber is larger in the transversal direction than in the
374 longitudinal direction: over the relative humidity range from 0% to 100% at 23 °C, a single cellulose fiber
375 roughly expanded by 1% in the longitudinal direction, whereas it expanded about 20 to 30% in the radial
376 direction (Wainwright, Biggs, & Currey, 1982). Thus, the strain of filament is mainly a radial strain, which
377 suggests that most of the cellulose fibers were aligned in the extrusion flow direction, as shown in Figure
378 5.

379 Figure 5B and D show SEM images of the inner structure of a filament dried with or without ethanol,
380 respectively. In both cases, a porous phase was present. This suggests that the deformation ends before
381 the end of the drying phase. Thus, the stiffness of the partially dried paste was sufficient to resist the
382 drying forces. Moreover, the characteristics of the porous phase were dependent of the drying process.
383 More pores were observed on the cross-section of the dried filament with ethanol exchange than on the
384 cross-section of the air-dried filament. This produced a larger diameter for the filament with the ethanol
385 bath, as is shown in Figure 5A and C. Indeed, the diameter of the dried filament with ethanol exchange

386 decreased from 0.72 to 0.56 ± 0.2 mm, whereas the dried filament without ethanol exchange decreased
387 from 0.72 to 0.49 ± 0.1 mm for the same set of extruded filaments. This improvement is a consequence
388 of the lower surface tension of ethanol compared to that of water (22 vs 72 mN m⁻¹, respectively)
389 resulting in a capillary pressure that was three times lower during the drying phase. This resulted in a
390 lower density for the filament with ethanol exchange after drying: 0.8 (with ethanol exchange) vs 1.1
391 (without ethanol exchange) g.cm⁻³.

392

393 3.2.3 Microstructure of the extruded filament



394

395 Figure 5. SEM images of the surface and cross-section of an (A, B) air dried filament and (C, D) air dried
396 filament with ethanol exchange.

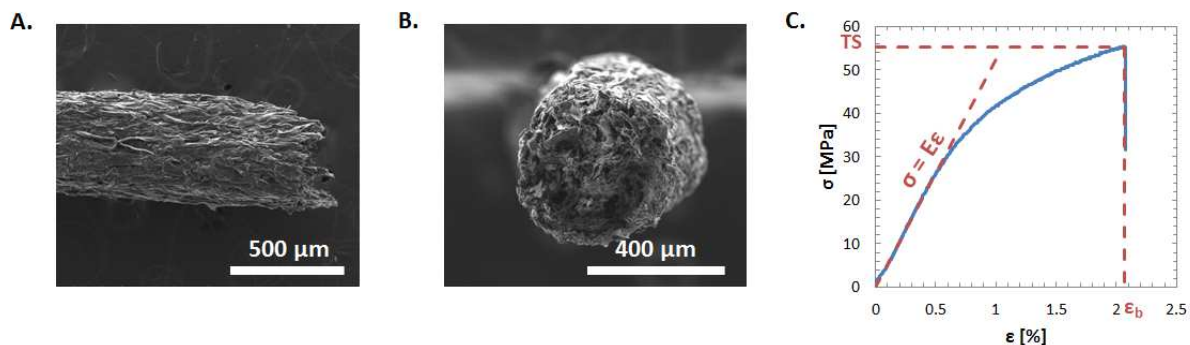
397 As shown in Figure 5A and C, the cellulosic fibers were mainly aligned in the extrusion direction,
398 independent of the drying technique used. These alignments may have been enhanced by the capillary
399 forces during the drying process.

400 The filament cross-sections are shown in Figures 5B and D, showing homogeneous solid phases where
401 only the cross section of the cellulosic fibers can be seen. The characteristics of the porous phase were
402 dependent on the drying process.

403 These last observations confirmed the following: (i) The initial paste was homogeneous due to the
404 mixing process that kept the cellulose fibers dispersed in this gelatinous matrix, forming a single phase
405 paste. (ii) The flow through the 0.7 mm nozzle was homogeneous, as no fiber aggregation or
406 detachment was observed, despite a mean cellulose fiber width of 27 μm for cellulose fibers with
407 lengths larger than 100 μm . This may have been owing to the CMC. Indeed, the addition of CMC
408 dissolved in water in the formulation acted as a gelation agent by increasing the water viscosity (Edali,
409 Esmail, & Vatisstas, 2001) and allowed the cellulose fibers to be embedded, which reduced the friction
410 between fibers. (iii) High stresses developed in the nozzle due to the elongational strain and shear rate
411 caused by the successive constrictions inside the nozzle and its small outlet diameter. For instance, the
412 apparent shear rate value was 10^1 - 10^2 s^{-1} for a flow rate of 5 mm s^{-1} through nozzles with outlet
413 diameters of 0.5–0.7 mm. These high stresses might be the main factor that induced fiber alignment.

414

415 **3.2.4 Tensile properties of the filament**



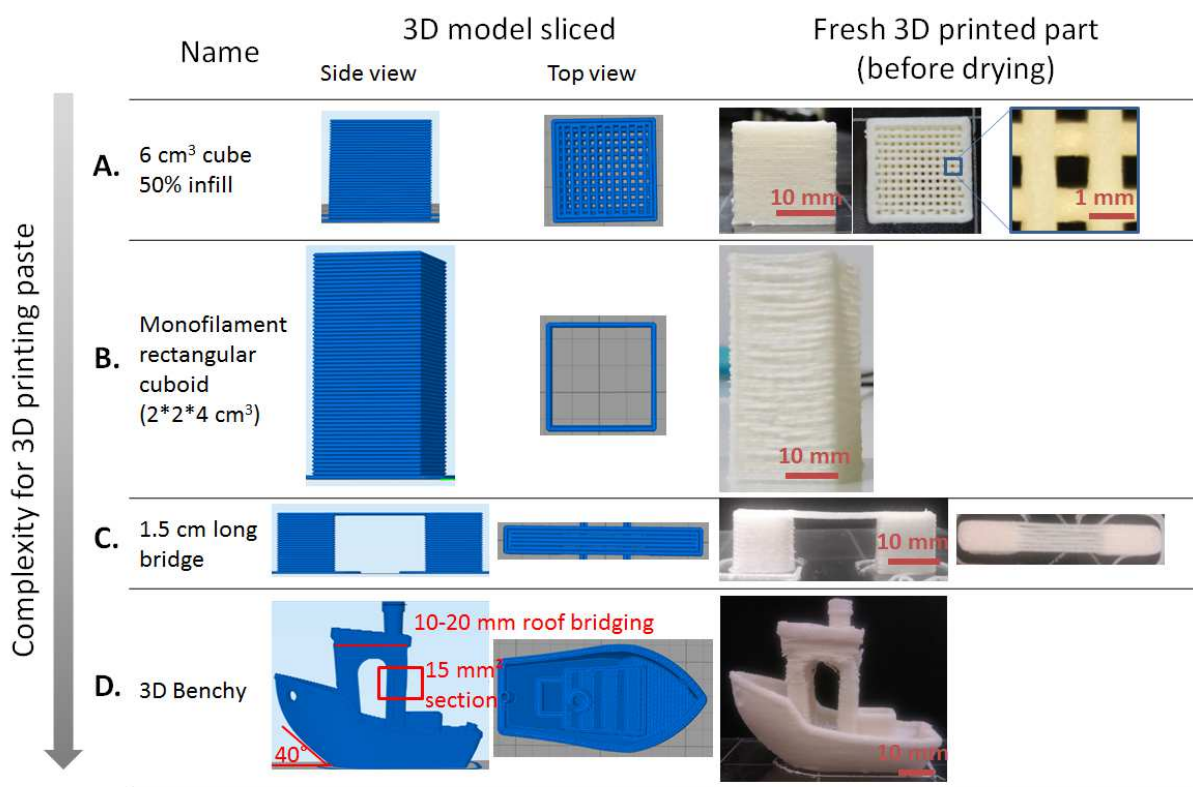
416
 417 Figure 6. SEM images of a fractured air dried filament extruded through a 0.7 mm nozzle diameter: (A)
 418 surface and (B) cross-section. (C) Typical stress-strain curve obtained for a tested air-dried filament.

419 Figure 6A and B show the fractured surfaces in the rupture zone of an air-dried filament after the
 420 tensile test. The cross-section of the filament after fracture was not sharp as those shown in Figure 5,
 421 indicating that some fibers broke away from the surrounding fibers. The strain stress curve obtained
 422 from the tensile test of a dried filament shown in Figure 6C is typical of the behavior of a brittle material
 423 without a strain-hardening region. From this strain-stress curve, the Young's modulus can be
 424 determined. For the air-dried filament, the Young's modulus was 5.4 ± 0.5 GPa, whereas the Young's
 425 modulus of the ethanol exchange dried filament was two times lower, with a value of 2.7 ± 0.3 GPa. This
 426 difference in stiffness was partially due to the higher porosity (42%) of the air dried filament with the
 427 ethanol bath compared to that (30%) of the air dried one without the ethanol bath, as illustrated in
 428 Figure 5B and D and calculated from their densities. However, such a difference in the Young's moduli
 429 cannot only be explained by the difference in porosities and presence of defects below the image
 430 resolution. Indeed, if we consider that the ethanol exchange dried filament had the same diameter as
 431 the air dried filament, the Young's modulus was about 3.5 ± 0.5 GPa, which is still lower than the 5.4 ± 0.5
 432 GPa of the air dried filament. Thus, the ethanol does not only affect the strain during drying, but it also
 433 might influence the hydrogen bonding between the cellulose fibers (Przybysz, Dubowik, Kucner,
 434 Przybysz, & Buzala, 2016) or the CMC-cellulose fiber adhesion.

435 The Young's moduli of the dried filaments were of the same order of magnitude as tensile test
 436 specimens of PLA using the Fused Filament Fabrication process, which range from 2 to 3 GPa according
 437 to the PLA data sheet of Stratasys, Ltd. This reinforces the hypothesis that this new cellulosic paste is
 438 compatible with the market expectations.

3.3 3D model printability

3.3.1 Fresh model



441
 442 Figure 7. 3D parts in order of increasing 3D printing complexity from (A) a cube to (D) the 3DBenchy. The
 443 side and top views of each 3D model slice and the corresponding printed cellulose part after completion
 444 are presented.

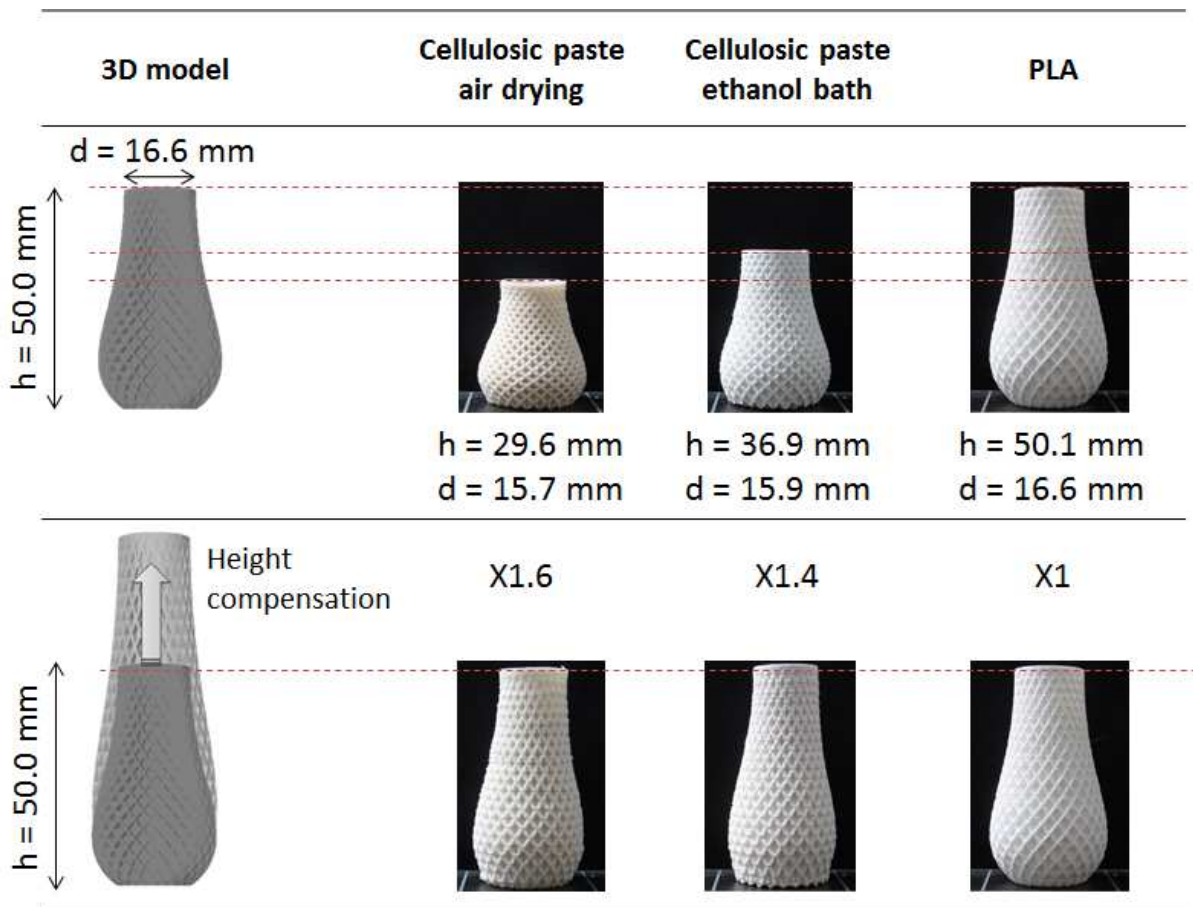
445 Figure 7 illustrates the 3D sliced models and fresh 3D printed part corresponding to the printing
 446 parameters presented in Table 1 using the optimized formulation. First, we fully succeeded in printing a

447 6 cm³ cube with 50% filling and two perimeter shells using a nozzle with a diameter of 0.7 mm (Figure
448 7A). The double perimeter wall of the printed cube appeared straight, and the inner grid was well
449 defined with a 6% standard deviation of the hole sizes. The successfully printed monofilament wall
450 cuboid, which was presented earlier, is shown again in Figure 7B. While there was a low contact surface
451 area (58 mm²) between the build platform and the first layer, there was a good adhesion during printing
452 whereas for the FFF printing of thermoplastics, care must be taken to obtain a good adhesion (such as
453 the temperature of the build platform) (Spoerk, Gonzalez-Gutierrez, Sapkota, Schuschnigg, & Holzer,
454 2018). A more complex 3D model was implemented to characterize the bridging capacity of the paste.
455 Figure 7C shows a successfully printed 15 mm long bridge. The success in printing this part was in one
456 hand due to the paste characteristics, such as restoring its strength just after exiting the nozzle. The
457 bridge remained straight after printing because the stress levels in the fresh state were below $|\sigma_y|$.
458 Using the Euler-Bernoulli beam theory and assuming that the filament behaves as a straight beam
459 clamped at its extremities under its own weight, the maximal tension-compression stresses in the
460 filament (located at its extremities) is $|\sigma_{\max}| = 2\rho g L^2 / 3d_f \approx 3.4$ kPa, which is below the value of 6 kPa
461 given in Figure 4D. The successful printing of this part was also due to the extrusion flow rate
462 adjustment. A flow rate that is too large will cause sagging of the suspended part of the bridge, whereas
463 a flow rate that is too small will result in filament breaking. For the most complex model, the 3DBenchy
464 (Figure 7.D), which took about 1 h to print, the 40° overhang using a nozzle diameter of 0.5 mm, and a
465 layer height of 0.3 mm (i.e. 50% of the width of the unsupported filament), exhibited no apparent
466 defects. However, the four 10 cm high pillars with smaller sections (<15 mm²) were not printed well.
467 Indeed, the pillars were flexible and moved with the printing head, resulting in crooked pillars. Unlike
468 thermoplastics that become rigid upon cooling, the paste used herein requires drying to become stiffer
469 to resist rapid motion of the nozzle on small surfaces. The bridging between the flexible pillars required
470 several layers (~5) to stiffen the structure and allow printing without defects.

471

472 **3.3.2 Model after drying**

473



474

475 Figure 8. 3D printing of a double spiral vase with the optimized formulation dried with or without an
476 ethanol bath or with polylactic acid (PLA). Upper row: 50 mm high vase. Lower row: vase with height
477 compensation in the model based on the calculated strain.

478 Figure 8 shows 3D printed solid vases with the optimized paste or with polylactic acid (PLA). The vases
479 in the first row of Figure 8 were printed with the same 3D model. As expected, the vase printed with PLA
480 maintained shape fidelity, as it did not exhibit any dimensional variations from the model. When printed

481 with the optimized paste, the air-dried model exhibited height and external diameter outlet strains of
482 41% and 5%, respectively. These strains decreased to 26% and 4%, respectively, by the addition of an
483 ethanol bath before air drying. The height strain of the vase was larger than the radial strain measured
484 on a single filament (c.f. Section 3.2.2). This may have been due to (i) the subsidence of the first layers
485 due to an overhang of 45° with almost 60% of the filaments unsupported, (ii) the addition of a load
486 during drying due the weight of the layers pressing down on the lower layer, and (iii) a larger drying time
487 due to a smaller surface contact and greater volume compared to those of a filament. The strain of the
488 external diameter outlet was a combination of length and radial strains of the filament. These strains,
489 mainly observed in the vertical plan of the part, enable us to devise a strategy to directly compensate for
490 the height change by introducing a height compensation in the digital 3D model to obtain a printed and
491 solid (dried) part with the desired height. The results are shown in Figure 8. With a multiplier coefficient
492 of 1.6, a printed vase similar to the one produced using fused filament fabrication with PLA was
493 achieved. This multiplier coefficient in height on the digital model was slightly lower than the calculated
494 strain for the 50 mm high vase (-5%). This may be due to (i) no subsidence of the first layer of the 80 mm
495 high vase due to a lower overhang of 32° and (ii) a compensation of the height strain due to slow drying
496 during the printing (printing time $\times \sim 1.6$). However, this compensation approach becomes less practical
497 for printing larger objects. Therefore, the solvent exchange (water- \rightarrow ethanol), which minimized the
498 radial strain of the filament, may be a good option for reducing dimension changes upon drying. Indeed,
499 the 3D printed 50 mm high vase immersed in ethanol after completion showed a significantly lower
500 strain, with only 26% height strain compared to the 41% strain for the non-immersed part. In this case, a
501 multiplier coefficient of 1.4 was used to compensate for the drying strain (Figure 8).

502

503 **4. Conclusion**

504 In this work, an innovative bio-based material for 3D printing by extrusion with a low-cost drying
505 solution was developed. A formulation with a high solid content was optimized based on specific criteria
506 to ensure accuracy between the cellulose printed part and the 3D model: (i) filament extrusion, (ii)
507 manufacturing accuracy, and (iii) limiting and forecasting deformation after drying. We proposed a paste
508 with a cellulose fiber content of 30 wt.%, a CMC content of 12.5 wt.%, and 57.5 wt.% of distilled water.
509 This paste exhibited a pronounced thinning behavior and a yield stress after relaxation, which are critical
510 parameters for 3D printing parts. Moreover, homogeneous filaments that exhibited high Young's moduli
511 (~5 GPa) in a dry state were produced by a screw-driven device with nozzle diameters ranging from 0.9
512 to 0.5 mm. This allowed the 3D printing of complex geometries. Design limitations linked to the printing
513 of tall and thin elements, such as the 10 mm high pillar with a cross-section of 15 mm², were identified.
514 A strategy to limit the isotropic deformation during air drying was proposed by adding a water-to-
515 ethanol exchange step after printing the fresh part. This decreased the shrinkage by one third from 36%
516 to 24% on average and divided the Young's modulus by two. These results emphasized that cellulose has
517 a strong potential to be used as a material for 3D printing with the promise of producing cheap,
518 lightweight, robust, and recyclable parts.

519

520 **Acknowledgements**

521 This work was supported by the Idex UGA grant (AGIR). The LGP2 and 3SR laboratories are part of the
522 LabEx Tec 21 (Investissements d'Avenir: grant agreement no. ANR-11-LABX-0030) and the PolyNat
523 Carnot Institute (Investissements d'Avenir: grant agreement no. ANR-16-CARN-0025-01). This research
524 was possible owing to the facilities of the TekLiCell platform funded by the Région Rhône-Alpes (ERDF:
525 European Regional Development Fund).

526 **References**

527 ASTM International. (2012). *Standard terminology for additive manufacturing technologies: designation*
528 *F2792-12a*. West Conshohocken, PA: ASTM International.

529 Buswell, R. A., Leal de Silva, W. R., Jones, S. Z., & Dirrenberger, J. (2018). 3D printing using concrete
530 extrusion: A roadmap for research. *Cement and Concrete Research*, *112*, 37–49.
531 <https://doi.org/10.1016/j.cemconres.2018.05.006>

532 Chalencon, F., Orgéas, L., Dumont, P. J. J., Foray, G., Cavallé, J.-Y., Maire, E., & Rolland du Roscoat, S.
533 (2010). Lubricated compression and X-ray microtomography to analyse the rheology of a fibre-
534 reinforced mortar. *Rheologica Acta*, *49*(3), 221–235. [https://doi.org/10.1007/s00397-009-0393-](https://doi.org/10.1007/s00397-009-0393-5)
535 [5](https://doi.org/10.1007/s00397-009-0393-5)

536 Chinga-Carrasco, G., Ehman, N. V., Pettersson, J., Vallejos, M. E., Brodin, M. W., Felissia, F. E., ... Area, M.
537 C. (2018). Pulping and pretreatment affect the characteristics of bagasse inks for three-
538 dimensional printing. *ACS Sustainable Chemistry & Engineering*, *6*(3), 4068–4075.
539 <https://doi.org/10.1021/acssuschemeng.7b04440>

540 Compton, B. G., & Lewis, J. A. (2014). 3D-printing of lightweight cellular composites. *Advanced Materials*
541 *(Deerfield Beach, Fla.)*, *26*(34), 5930–5935. <https://doi.org/10.1002/adma.201401804>

542 Crump, S. S. (1992). *US5121329A*. United States. Retrieved from
543 <https://patents.google.com/patent/US5121329/en>

544 Dai, L., Cheng, T., Duan, C., Zhao, W., Zhang, W., Zou, X., ... Ni, Y. (2019). 3D printing using plant-derived
545 cellulose and its derivatives: A review. *Carbohydrate Polymers*, *203*, 71–86.
546 <https://doi.org/10.1016/j.carbpol.2018.09.027>

547 Dufresne, A. (2013). *Nanocellulose: From nature to high performance tailored materials*. Walter de
548 Gruyter.

549 Edali, M., Esmail, M. N., & Vatistas, G. H. (2001). Rheological properties of high concentrations of
550 carboxymethyl cellulose solutions. *Journal of Applied Polymer Science*, 79(10), 1787–1801.
551 [https://doi.org/10.1002/1097-4628\(20010307\)79:10<1787::AID-APP70>3.0.CO;2-2](https://doi.org/10.1002/1097-4628(20010307)79:10<1787::AID-APP70>3.0.CO;2-2)

552 Eqtesadi, S., Motealleh, A., Miranda, P., Lemos, A., Rebelo, A., & Ferreira, J. M. F. (2013). A simple recipe
553 for direct writing complex 45S5 Bioglass® 3D scaffolds. *Materials Letters*, 93, 68–71.
554 <https://doi.org/10.1016/j.matlet.2012.11.043>

555 Feygin, M., & Hsieh, B. (1991). Laminated Object Manufacturing (LOM): a simpler process.
556 <https://doi.org/10.15781/T2PV6BQ54>

557 Håkansson, K. M. O., Henriksson, I. C., de la Peña Vázquez, C., Kuzmenko, V., Markstedt, K., Enoksson, P.,
558 & Gatenholm, P. (2016). Solidification of 3D printed nanofibril hydrogels into functional 3D
559 cellulose structures. *Advanced Materials Technologies*, 1(7), n/a-n/a.
560 <https://doi.org/10.1002/admt.201600096>

561 Huang, S. H., Liu, P., Mokasdar, A., & Hou, L. (2013). Additive manufacturing and its societal impact: a
562 literature review. *The International Journal of Advanced Manufacturing Technology*, 67(5),
563 1191–1203. <https://doi.org/10.1007/s00170-012-4558-5>

564 Jia, C., Bian, H., Gao, T., Jiang, F., Kierzewski, I. M., Wang, Y., ... Hu, L. (2017). Thermally stable cellulose
565 nanocrystals toward high-performance 2D and 3D nanostructures. *ACS Applied Materials &*
566 *Interfaces*, 9(34), 28922–28929. <https://doi.org/10.1021/acsami.7b08760>

567 Klar, V., Kärki, P., Orelma, H., & Kuosmanen, P. (2017). Analysis of drying deformation of 3D printed
568 nanocellulose structures. In *Cellulose Materials Doctoral Students Conference 2017*. Graz
569 University of Technology, TUG. Retrieved from
570 [https://research.aalto.fi/en/publications/analysis-of-drying-deformation-of-3d-printed-](https://research.aalto.fi/en/publications/analysis-of-drying-deformation-of-3d-printed-nanocellulose-structures(447440d2-bf95-47bb-98ab-f9984beb3f4a).html)
571 [nanocellulose-structures\(447440d2-bf95-47bb-98ab-f9984beb3f4a\).html](https://research.aalto.fi/en/publications/analysis-of-drying-deformation-of-3d-printed-nanocellulose-structures(447440d2-bf95-47bb-98ab-f9984beb3f4a).html)

572 Lewis, J. A. (2006). Direct ink writing of 3D functional materials. *Advanced Functional Materials*, 16(17),
573 2193–2204. <https://doi.org/10.1002/adfm.200600434>

574 Li, L., Zhu, Y., & Yang, J. (2018). 3D bioprinting of cellulose with controlled porous structures from
575 NMMO. *Materials Letters*, 210, 136–138. <https://doi.org/10.1016/j.matlet.2017.09.015>

576 Li, V. C. F., Mulyadi, A., Dunn, C. K., Deng, Y., & Qi, H. J. (2018). Direct ink write 3D printed cellulose
577 nanofiber aerogel structures with highly deformable, shape recoverable, and functionalizable
578 properties. *ACS Sustainable Chemistry & Engineering*, 6(2), 2011–2022.
579 <https://doi.org/10.1021/acssuschemeng.7b03439>

580 Li, V. C. F., Dunn, C. K., Zhang, Z., Deng, Y., & Qi, H. J. (2017). Direct Ink Write (DIW) 3D printed cellulose
581 nanocrystal aerogel structures. *Scientific Reports*, 7(1), 8018. [https://doi.org/10.1038/s41598-](https://doi.org/10.1038/s41598-017-07771-y)
582 [017-07771-y](https://doi.org/10.1038/s41598-017-07771-y)

583 Markstedt, K., Mantas, A., Tournier, I., Martínez Ávila, H., Hägg, D., & Gatenholm, P. (2015). 3D
584 bioprinting human chondrocytes with nanocellulose-alginate bioink for cartilage tissue
585 engineering applications. *Biomacromolecules*, 16(5), 1489–1496.
586 <https://doi.org/10.1021/acs.biomac.5b00188>

587 Markstedt, K., Sundberg, J., & Gatenholm, P. (2014). 3D bioprinting of cellulose structures from an ionic
588 liquid. *3D Printing and Additive Manufacturing*, 1(3), 115–121.
589 <https://doi.org/10.1089/3dp.2014.0004>

590 Martoia, F., Perge, C., Dumont, P. J. J., Orgéas, L., Fardin, M. A., Manneville, S., & Belgacem, M. N.
591 (2015). Heterogeneous flow kinematics of cellulose nanofibril suspensions under shear. *Soft*
592 *Matter*, 11(24), 4742–4755. <https://doi.org/10.1039/c5sm00530b>

593 Nguyen, D., Hägg, D. A., Forsman, A., Ekholm, J., Nimkingratana, P., Brantsing, C., ... Simonsson, S.
594 (2017). Cartilage tissue engineering by the 3D bioprinting of iPS cells in a nanocellulose/Alginate
595 Bioink. *Scientific Reports*, 7(1), 658. <https://doi.org/10.1038/s41598-017-00690-y>

596 Orgéas, L., Gabathuler, J.-P., Imwinkelried, T., Paradies, C., & Rappaz, M. (2003). Modelling of semi-solid
597 processing using a modified temperature-dependent power-law model. *Modelling and*
598 *Simulation in Materials Science and Engineering*, 11(4), 553. [https://doi.org/10.1088/0965-](https://doi.org/10.1088/0965-0393/11/4/309)
599 [0393/11/4/309](https://doi.org/10.1088/0965-0393/11/4/309)

600 Orgéas, L., Dumont, P. J. J., Le, T.-H., & Favier, D. (2008). Lubricated compression of BMC, a concentrated
601 and fibre-reinforced granular polymer suspension. *Rheologica Acta*, 47(5), 677.
602 <https://doi.org/10.1007/s00397-008-0276-1>

603 Passas, R., Voillot, C., Tarrajat, G., Khélifi, B., Pétot, E. & Tourtollet, G. (2001). MorFi : analyseur
604 morphologique des fibres. (2001),SFGP

605 Pattinson Sebastian W., & Hart A. John. (2017). Additive manufacturing of cellulosic materials with
606 robust mechanics and antimicrobial functionality. *Advanced Materials Technologies*, 2(4),
607 1600084. <https://doi.org/10.1002/admt.201600084>

608 Przybysz, P., Dubowik, M., Kucner, M. A., Przybysz, K., & Buzafa, K. P. (2016). Contribution of hydrogen
609 bonds to paper strength properties. *PLOS ONE*, 11(5), e0155809.
610 <https://doi.org/10.1371/journal.pone.0155809>

611 Rees, A., Powell, L. C., Chinga-Carrasco, G., Gethin, D. T., Syverud, K., Hill, K. E., & Thomas, D. W. (2015).
612 3D bioprinting of carboxymethylated-periodate oxidized nanocellulose constructs for wound
613 dressing applications. <https://doi.org/10.1155/2015/925757>

614 Sachs, E., Cima, M., Williams, P., Brancazio, D., & Cornie, J. (1992). Three dimensional printing: rapid
615 tooling and prototypes directly from a CAD model. *Journal of Engineering for Industry*, 114(4),
616 481–488. <https://doi.org/10.1115/1.2900701>

617 Sanandiya, N. D., Vijay, Y., Dimopoulou, M., Dritsas, S., & Fernandez, J. G. (2018). Large-scale additive
618 manufacturing with bioinspired cellulosic materials. *Scientific Reports*, 8(1), 8642.
619 <https://doi.org/10.1038/s41598-018-26985-2>

620 Scherer, G. W. (1990). Theory of drying. *Journal of the American Ceramic Society*, 73(1), 3–14.
621 <https://doi.org/10.1111/j.1151-2916.1990.tb05082.x>

622 Siqueira, G., Kokkinis, D., Libanori, R., Hausmann, M. K., Gladman, A. S., Neels, A., Studart, A. R. (2017).
623 Cellulose nanocrystal inks for 3D printing of textured cellular architectures. *Advanced Functional*
624 *Materials*, 27(12), n/a-n/a. <https://doi.org/10.1002/adfm.201604619>

625 Smay, J. E., Cesarano, J., & Lewis, J. A. (2002). Colloidal inks for directed assembly of 3-D periodic
626 structures. *Langmuir*, 18(14), 5429–5437. <https://doi.org/10.1021/la0257135>

627 Spoerk, M., Gonzalez-Gutierrez, J., Sapkota, J., Schuschnigg, S., & Holzer, C. (2018). Effect of the printing
628 bed temperature on the adhesion of parts produced by fused filament fabrication. *Plastics,*
629 *Rubber and Composites*, 47(1), 17–24. <https://doi.org/10.1080/14658011.2017.1399531>

630 Steinle, P. (2016). Characterization of emissions from a desktop 3D printer and indoor air measurements
631 in office settings. *Journal of Occupational and Environmental Hygiene*, 13(2), 121–132.
632 <https://doi.org/10.1080/15459624.2015.1091957>

633 Suiker, A. S. J. (2018). Mechanical performance of wall structures in 3D printing processes: Theory,
634 design tools and experiments. *International Journal of Mechanical Sciences*, 137, 145–170.
635 <https://doi.org/10.1016/j.ijmecsci.2018.01.010>

636 Sultan, S., & Mathew, A. P. (2018). 3D printed scaffolds with gradient porosity based on a cellulose
637 nanocrystal hydrogel. *Nanoscale*, 10(9), 4421–4431. <https://doi.org/10.1039/c7nr08966j>

638 Thingiverse.com. (n.d.). Thingiverse - Digital Designs for Physical Objects. Retrieved March 13, 2018,
639 from <https://www.thingiverse.com/>

640 Wainwright, S. A., Biggs, W. D., & Currey, J. D. (1982). *Mechanical design in organisms*. Princeton
641 University Press.

642 Wang, Q., Sun, J., Yao, Q., Ji, C., Liu, J., & Zhu, Q. (2018). 3D printing with cellulose materials. *Cellulose*,
643 25(8), 4275–4301. <https://doi.org/10.1007/s10570-018-1888-y>

644 Wittbrodt, B., & Pearce, J. M. (2015). The effects of PLA color on material properties of 3-D printed
645 components. *Additive Manufacturing, 8*, 110–116.

646 <https://doi.org/10.1016/j.addma.2015.09.006>

647 Wohlers, T. , Caffrey, T. &, Campbell, I. (2016). *Wohlers report 2016: 3D printing and additive*
648 *manufacturing state of the industry : Annual Worldwide Progress Report*. Wohlers Associates.

649